Materials and Design 191 (2020) 108650

Contents lists available at ScienceDirect

Materials and Design

journal homepage: www.elsevier.com/locate/matdes

Poly-para-xylylene enhanced Fe-based amorphous powder cores with improved soft magnetic properties via chemical vapor deposition

Yiqun Zhang [a,b], Yaqiang Dong [a,b,*], Bang Zhou [a], Qiang Chi [a], Liang Chang [a], Mengji Gong [a], Jianjun Huang [a], Yan Pan [a], Aina He [a,b], Jiawei Li [a,b], Xinmin Wang [a]

[a] Zhejiang Province Key Laboratory of Magnetic Materials and Application Technology, CAS Key Laboratory of Magnetic Materials and Devices, Ningbo Institute of Materials Technology & Engineering, Chinese Academy of Sciences, Ningbo, Zhejiang 315201, China
[b] University of Chinese Academy of Sciences, Beijing 100049, China

HIGHLIGHTS

- Poly-para-xylylene has first designed as coating layer for amorphous powder cores.
- Three layer thickness has been designed and estimated by several methods.
- APTES can enhance binding force between coating layer and powder.
- The powder cores show high DC bias performance (54.3%) and low P_{cv} (770 mW/cm^3).

GRAPHICAL ABSTRACT

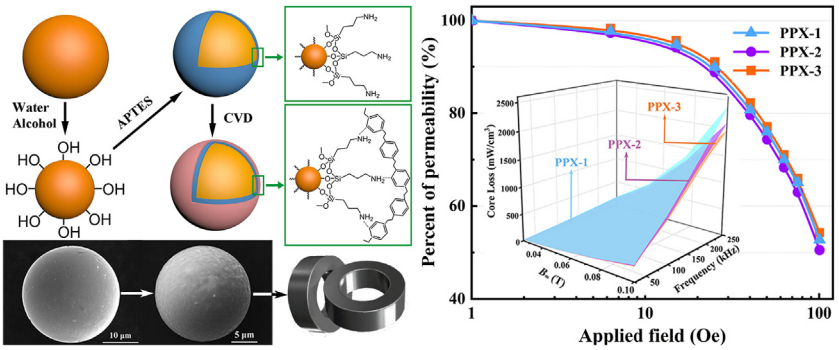

ARTICLE INFO

Article history:
Received 7 January 2020
Received in revised form 15 March 2020
Accepted 16 March 2020
Available online xxxx

Keywords:
Amorphous powder cores
Poly-para-xylylene
Core loss
DC bias performance

ABSTRACT

In this work, dense and pinhole-free poly-para-xylylene (PPX) with high thermal stability, high insulating property and high lubricity has been designed as coating layer for Fe-based amorphous powder. Three ultra-thin PPX layers have been successfully deposited on the surface of FeSiBPNbCr amorphous powder via chemical vapor deposition (CVD) polymerization. The micromorphology and chemical structure of the PPX layer on the powder surface, as well as the conversion mechanisms, has been investigated systematically. Several methods have been used to estimate the amount and thickness of PPX layers. The corresponding amorphous powder cores (AMPCs) were also prepared. With the increasing thickness of the PPX layer, the saturation magnetization (M_s) of the powder decreased slightly but the magnetic flux density (B_s) of the AMPCs kept at a similar level thanked to the enhanced green density. In addition, the DC bias performance was improved and core loss (P_{cv}) was reduced. Compare with other coating materials like epoxy and silicon resin, the PPX layer provided better insulation and higher lubricity for the AMPCs, thus reduced the P_{cv} and improved the DC bias performance. The AMPCs coated by PPX-3 exhibited excellent comprehensive soft magnetic properties, which were promising for high-power and high-frequency applications.

* Corresponding author at: Zhejiang Province Key Laboratory of Magnetic Materials and Application Technology, CAS Key Laboratory of Magnetic Materials and Devices, Ningbo Institute of Materials Technology & Engineering, Chinese Academy of Sciences, Ningbo, Zhejiang 315201, China.
E-mail address: dongyq@nimte.ac.cn (Y. Dong).

https://doi.org/10.1016/j.matdes.2020.108650

1. Introduction

Soft magnetic materials, which are composed of silicon steel, soft magnetic composites (SMCs) and soft ferrites, play a key role in the conversion of energy throughout the world [1]. Traditional silicon steels exhibit high magnetic flux density (B_s) over 2.0 T, but the huge eddy current losses (P_e) limits the working frequency [2]. Soft ferrites with high electrical resistivity work well in the megahertz frequency range, but their B_s is less than 0.5 T [3]. SMCs have been constructed by the micro or nano magnetic powder mixed with insulation materials, and then consolidated by high pressure. The working frequency and B_s of SMCs are between steel and ferrites, which just fill the gap between them [4].

As a new generation of electric alloys, amorphous alloys have proved to exhibit high hardness, high resistivity, high permeability, low coercivity (H_c) and anti-corrosion thanks to the amorphous structure [5], which render them become a suitable core materials for SMCs [6,7]. High strength is one of the most significant and unique mechanical characteristics of amorphous alloys. The $(Fe_{0.335}Co_{0.335}Nb_{0.06}B_{0.27})_{99.8}Cu_{0.2}$ amorphous alloy attained the highest compressive fracture strength of 4930 MPa, which is ten times than general steel [8]. Once prepared in powder form, this unique advantage would become a drawback. The Vickers hardness (H_v) of Liqualloy™ (Fe-Cr-(B,P,Si,C)) amorphous powder is 980, which is twice as much as FeSiAl powder (H_v = 500) and 6.5 times harder than FeNi powder (H_v = 150) [9]. The high hardness of amorphous powder makes it difficult to be consolidated, the density of amorphous powder cores (AMPCs) is unsatisfactory if compressed via conventional pressure, only 4.6 g/cm^3 at 800 MPa [10]. Therefore, high pressure has been applied to the formation of the AMPCs, usually 1600–2500 MPa [11–13]. Inorganic coating materials such as phosphate, glass water and ferrite, are easily brittle rupture at such high pressure, which will damage the insulation performance [14]. For the in-situ grown oxides like Fe_3O_4, it is difficult to be dense and completely enveloped around the magnetic powder [15]. Organic materials such as epoxy, silicon, and phenolic resin, can completely wrap around the magnetic powder and maintain integrity under high pressure. However, the thermal decomposition temperature of resin is usually lower than 300 °C [11]. In order to maintain the strength of the powder cores, more resin should be used for compaction, thus the air gap between powders was increased as well as the hysteresis losses (P_h). In order to solve the existing problems, a kind of new insulating materials with superior insulating performance, high stability under high pressure, good fluidity and high temperature resistance is urgently needed.

Poly-para-xylylene (PPX, also called Parylene), which has been used for more than 30 years, is a kind of polymer that can be prepared in a solventless process via chemical vapor deposition (CVD) polymerization [16]. Conventional PPX coatings with excellent chemical inertness, low friction factor, high insulating performance, high thermal stability over 420 °C and excellent barrier properties, are typically used to provide an inert packaging that suppresses potential adverse effects stemming from the substrate [17]. PPX coating found its first application as a coating outside the ferrite cores of the electronics [18]. However, there are few studies on the PPX coating on the powder surface, especially fine powder. H.T. Pu et al. [19] have successfully deposited PPX layers for iron powder which are used for magnetorheological fluids, the morphology and chemical stability was investigated. Iron powder cores with PPX-C coating layer were successfully manufactured with enhanced density by S. Wu et al. [20]. However, none of the above works describes the key magnetic properties such as core loss (P_{cv}) and DC bias performance, nor does it compare with other powder cores.

In this work, the thin and uniform PPX coating layer was first designed as the coating layer for fine amorphous magnetic powder via CVD process. The micromorphology and chemical structure of the PPX layer on the powder surface, as well as the conversion mechanisms, has been investigated in details. Three different thickness has been designed for the coating layer; several methods have been used to estimate the thickness of coating layer. The influence of the thickness of the coating layer on the soft magnetic properties of the AMPCs was further explored. As a highlight, the high thermal stability and high lubricity of PPX layer could provide excellent soft magnetic properties for the AMPCs compared with other resin coated samples.

2. Experimental methods

2.1. Fabrication

The $Fe_{77}Si_4B_{10}P_6Nb_2Cr_1$ amorphous powder was prepared by water atomization and then sieved into 400 meshes, the detail process was similar to the method in our previous work [21].

Sieved amorphous powder was washed three times by alcohol and then modified by 1 wt% 3-triethoxysilypropylamine (APTES, 99 wt%, Aladdin Industrial Co.) in weakly acidic alcohol-water aqueous for 0.5 h through ultrasonic dispersion. Subsequently, the APTES surface functionalized amorphous powder was washed thoroughly with alcohol followed by drying in 60 °C in vacuum for 6 h before application. The CVD process of the powder was provided by Zasen Nano Tech Co. and the details were presented in Fig. 1. The amorphous powder was first set into the cylindrical container, which rotated with the deposition chamber. Then, paracyclophane (PCP) dimer sublimed in the sublimation zone, and the vaporized PCP gas cracked into activated monomers gas in pyrolyze zone. The reactive monomer gas finally condensed and polymerized on the surface of rotating powder in room temperature. Three different thickness layers have been successfully prepared. The corresponding samples were marked as PPX-1, PPX-2 and PPX-3, respectively. For comparison, the powder was also coated by 2 wt% epoxy resin (EP, W-6C) and two types of silicon resin (SR, REN 60 and JM 10). The washed amorphous powder was introduced into resin which dissolved in acetone. Then, the mixture was treated by an ultrasonic dual-mixing process of using ultrasonic vibration along with mechanical stirring by an impeller at room temperature. After the solvent was completely evaporated, the powder dried under vacuum at 60 °C for 2 h.

The as-coated amorphous powder was consolidated by a pressure-testing machine (Suns YAW-600) under a pressure of 1200–2000 MPa and dwell time of 60 s to obtain the toroidal Fe-based AMPCs (Φ 20.3 × φ 12.7 × 5.5 mm) at room temperature. For stress relaxation, the compacted AMPCs were set into the tube furnace, annealed at 460 °C for 1 h and cooled at room temperature for 1 h in vacuum.

2.2. Characterization

The morphology of the powder was examined by scanning electron microscopy (SEM, ZEISS EVO 18, Germany). Surface chemistry of the powder was measured by Fourier transform infrared (FTIR, Thermo Nicolet 6700, America) and X-ray photoelectron spectroscopy (XPS, Kratos Axis Ultra DLD, Japan). The thermal behavior was determined using a thermo-gravimeter analyzer (TG, PerkinElmer Diamond TG/DTA, America) in a nitrogen atmosphere. The particle size distribution was tested by laser particle size distribution instrument (Helos-oasis, Germany). The hysteresis loop was measured by vibrating sample magnetometer (VSM, Lakeshore7410, America) with a maximum applied field of 800 kA/m. The green density of the compacts was calculated from their weight and dimensions, and the true density was obtained by He pycnometer through gas true density analyzer (Builder TD-2200, China). Permeability spectra of the AMPCs were measured by an impedance analyzer (Agilent 4294A, America) from 1 kHz to 110 MHz. The P_{cv} of the samples was measured by broadband power analyzer (Clarke-hess Model 2335A, America), and the DC-bias performance was measured by an LCR meter (TongHui TH2828A, China) with 50 turns of copper wire twined tightly around the cores.

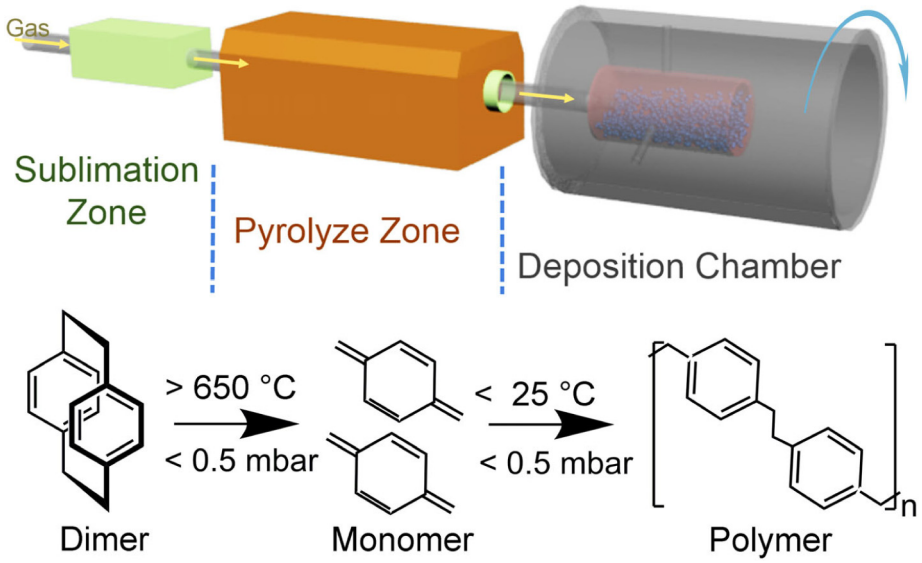

Fig. 1. Diagram of chemical vapor deposition polymerization of PPX.

3. Results and discussion

3.1. Micromorphology and chemical structure of the powder

Fig. 2 provided the SEM images of the amorphous powder coated by different PPX layers. A smooth surface of PPX-1 and PPX-2 was presented in Fig. 2(a) and (b). The PPX layers were evenly and compactly coated on the powder, no pinhole and defect can be observed on the surface even the layer was very thin. As the layer was further thickened in Fig. 2(c), the surface of the PPX-3 become rough, but still uniform and dense. The dense and pinhole-free layer was beneficial to completely block the eddy current between the powder, and thus reduce the P_{cv} of the AMPCs. The magnetic powder was hot inlayed through mosaic resin, the cross sections were obtained after polishing and the micrography was illustrated in Fig. 2(d)–(f). The average thickness of the PPX layers was gradually increased from PPX-1 to PPX-3, approximately 65, 140 and 240 nm, respectively. We found an interesting phenomenon in Fig. 2(g) that as the layer was thick, there excited a large layer wrapped with some small powder. Further magnification of the observations in Fig. 2(h) and (i) revealed that small powder inside have also been wrapped by PPX layers. However, this phenomenon was not seen in PPX-1 and PPX-2. The gas with PPX active monomer was slowly entered into the deposition chamber and deposited on tumbling amorphous powder. When PPX layer deposited on the amorphous powder was thick, some of the powder have been stuck together to form a large powder. Therefore, further introduction of the PPX reactive

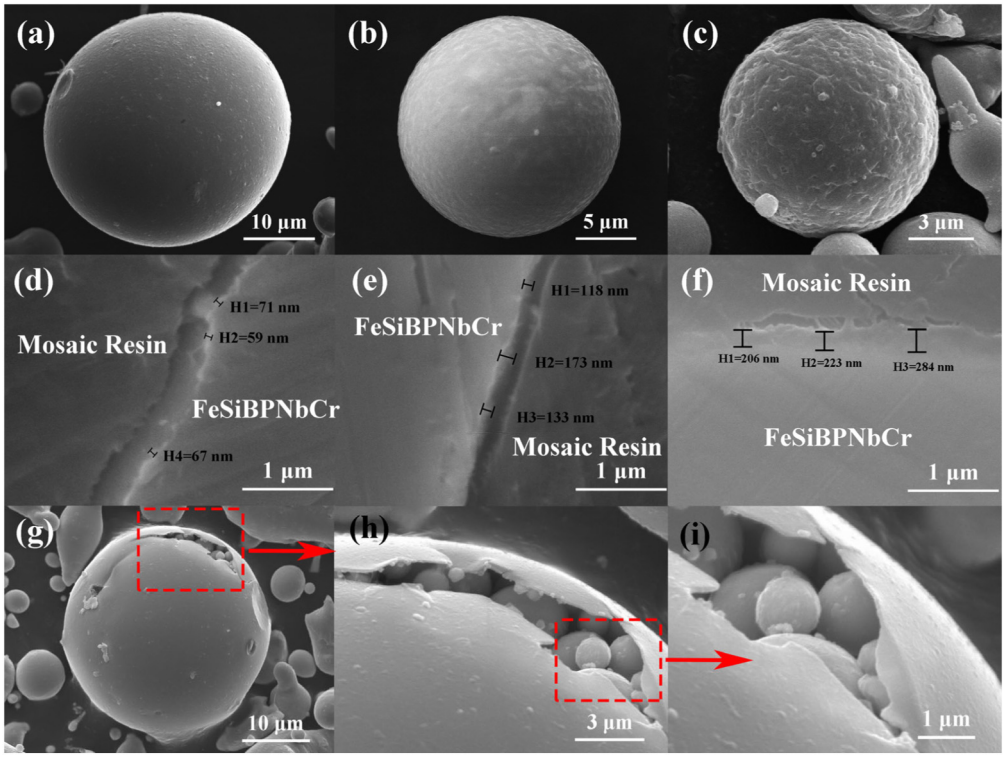

Fig. 2. SEM micrograph of the amorphous powder coated by (a) PPX-1, (b) PPX-2, (c, g–i) PPX-3, and the cross section of the powder coated by (d) PPX-1, (e) PPX-2 and (f) PPX-3.

monomer will result in the large agglomerated powder being wrapped by large PPX layer. Proper non-magnetic material coating is advantageous to reduce the P_e, however, further increased the amount of non-magnetic materials, the magnetic properties would be weakened such as sharp drop in B_s and permeability [22,23].

Surface chemistry of the powder was measured by FTIR and the spectra was shown in Fig. 3. Broad bands around at 3436 and 1630 cm^{-1} of every curve were observed clearly in both Fig. 3(a) and (b), which corresponded to the infrared absorption of the -OH group and resulted from water-absorption on the powder surface and hydrolyzed APTES. Weak peaks of 2920 and 2850 cm^{-1} originated from $-CH_2$ stretching vibration and the peak of 1384 cm^{-1} originated from two equal-intensity C—H deformation vibration. The peaks formed at 1065 cm^{-1} can be attributed to the stretching vibration of Si-O-Si and the weak peak at 899 cm^{-1} showed in the enlarged image origins from external deformation vibration of N—H [24]. However, there were no such peaks in the spectra of amorphous powder, indicating that the amorphous powder has been successfully modified by APTES. For powder coated by PPX, several additional absorption peaks were appeared. Peaks at 1512 and 820 cm^{-1} were attributed to the stretching vibration of benzene ring, and the peak of 820 cm^{-1} indicated that the benzene ring was replaced by the p-position. The peak at 542 cm^{-1} corresponding to the deformation vibration of =C-C-C [19,25]. Thus, it can be confirmed from FTIR spectra that the polymer covered outside the amorphous powder was the combination of APTES and PPX. However, as can be seen from the enlarged inset, the N—H vibration peak of 899 cm^{-1} on the spectra of APTES appeared at the 887 cm^{-1} on the PPX spectra. It indicated that there existed intermolecular forces between the $-NH_2$ in APTES and the PPX layer. The formation of intermolecular forces decreased the bond constant of the original chemical bond, and the absorption frequency shifted in the direction of the lower wave number [26]. FTIR spectra of the amorphous powder coated by different thicknesses of PPX were shown in Fig. 3(b), and the inset showed the details. The intensity of these peaks including 1512, 820, and 542 cm^{-1}, which related to benzene ring, were enhanced from PPX-1 to PPX-3. This result indicated that a thicker polymer layer has been wrapped around the amorphous powder.

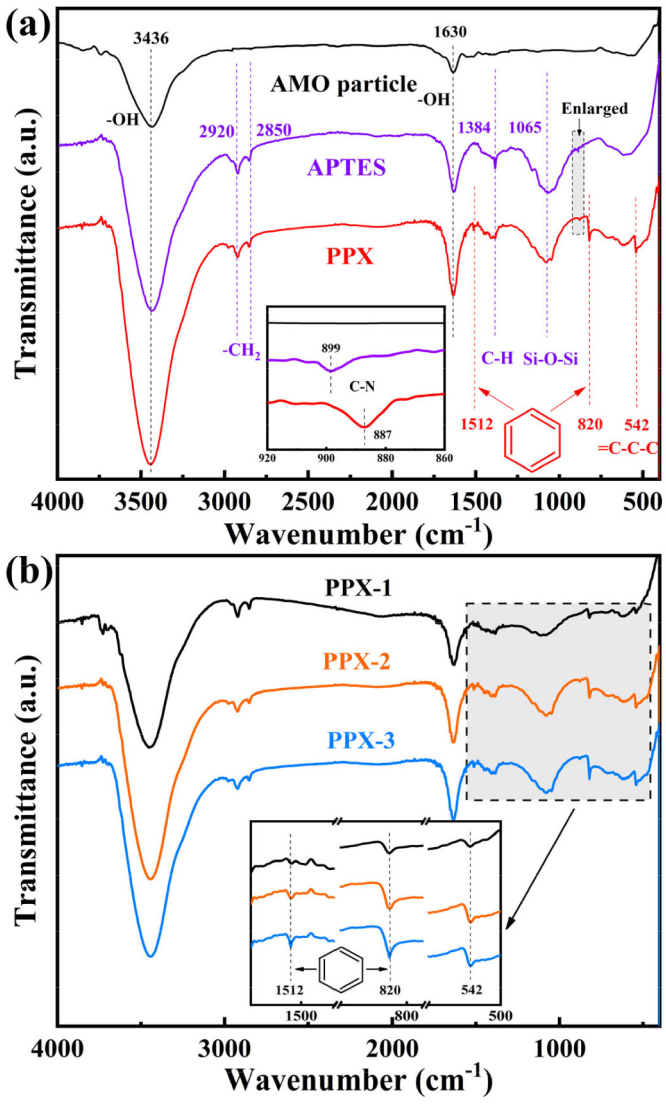

Fig. 3. FTIR patterns of (a) the amorphous powder and the powder coated by APTES and PPX, (b) the powder coated by different PPX layers.

To further investigate the chemical composition, XPS was carried out for the powder with different coating layer. Fig. 4(a) showed the survey XPS spectra of the amorphous powder and powder coated by APTES and PPX. The peaks apparent in survey spectra included C 1s, O 1s, N 1s, Si 2s and Si 2p peaks. Curve-fitted high-resolution XPS spectra of obtained samples were shown in Fig. 4(b)–(i). For the Si 2p spectra, only one peak appearing at 101.9 eV related to the silicones (Si—O and Si—C) [27]. For the C 1s spectra, at least three different carbon environments were found in APTES, as shown in Fig. 4(d), including: (1) hydrocarbon (C—C and C—H) at 284.8 eV; (2) amine (C—N) at 286.2 eV and (3) carbonyl (C=O) at 288.4 eV related to carbon dioxide in the air. However, there was a new peak appeared at 291.5 eV in the curve of PPX (Fig. 4(g)). Two main sources may contribute to the formation of this peak. The one is the binding energy of fluorocarbon (C—F) [28], but no fluorine here related to Fig. 4(c). Therefore, the new peak came from the shake up and was related to benzene ring structure, indicating that the PPX has been coated around the powder [29]. For the O 1s region in APTES, as shown in Fig. 4(e), three components are detected at 530.5, 532.2 and 533.6 eV, arising from the iron oxide (Fe—O), silicones (Si—O) and carbonyl (C=O), respectively [30]. After PPX coating, the binding energy of O 1s was basically unchanged compared Fig. 4(h) to (e). It indicated that the hydroxyl in APTES combined with the surface of the amorphous powder and form the Fe—O bond. Only one symmetric peak at 399.5 eV (C—N) was found for the N 1s region in APTES, as shown in Fig. 4(f). The C—N bond in PPX shifted to 399.8 eV in Fig. 4(i), indicating that the intermolecular force appeared between the $-NH_2$ in APTES and the PPX layer. These observations were particularly consistent with the results of FTIR.

Fig. 5 showed the XPS spectra of the C 1s, O 1s and N 1s peaks for the amorphous powder coated by different layers. Enhanced intensity of C 1s was observed from PPX-1 to PPX-3, indicating that the content of carbon in the surface was increasing. On the contrary, the intensity of O 1s and N 1s showed the opposite trend. These observations had obvious implications that the proportion of carbon was increased from PPX-1 to PPX-3, meanwhile, the proportion of oxygen and nitrogen decreased. It further proved that the thickness of the PPX layer was increasing.

The evolution of the coating layer can be speculated based on combining FTIR, XPS analysis and SEM microtopography, and was shown in Fig. 6. APTES is a commonly used amino coupling agent. After dissolving in slightly acidic ethanol solution, the APTES hydrolyze to silanol and Si-O-Si groups can be formed between the silanols. Since there exist substantial surface-to-volume atomic ratio and high surface activity of small powder surface, the atoms on the surface were apt to adsorb ions or molecules in solution. The amorphous powder scattered in a weakly acidic ethanol solution, the bare atoms of Fe on the powder surface would adsorb -OH groups, so there existed a -OH rich surface [24]. The -OH groups on the surface of amorphous powder dehydrated with the -OH groups of silanol. Since the terminal of APTES contained functional $-NH_2$ groups, the amorphous powder can be modified with rich $-NH_2$ groups by APTES through chemical bond. During the CVD process,

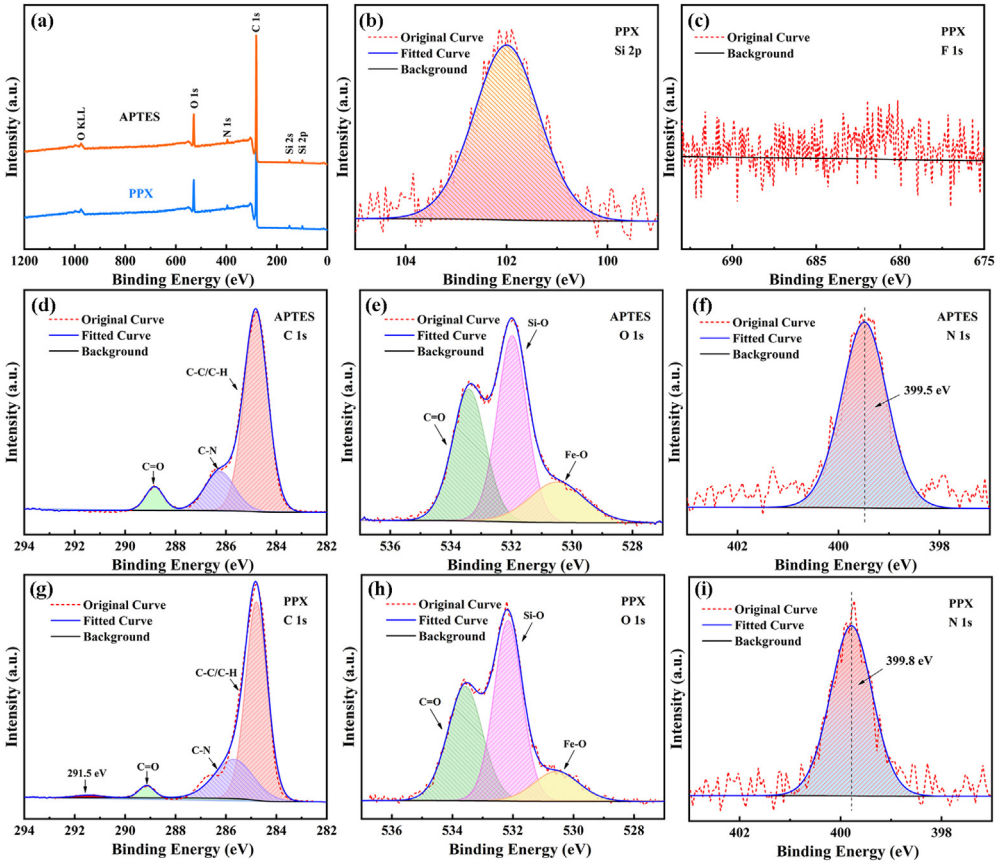

Fig. 4. XPS spectra of the powder surface layers.

vaporized PCP gas cracked into activated monomers and then deposited and polymerized at room temperature on the surface of amorphous powder [19]. As the carbon on the aromatic ring also has a relatively strong electron-absorbing ability, the PPX layer was connected to the amorphous powder through APTES, and the -NH_2 groups at the end of APTES generated intermolecular interactions with the benzene ring, thus enhancing the binding force between the layer and the powder [31].

3.2. The estimation of the amount and thickness of PPX layer

In order to estimate the amount of PPX layer on the surface of the amorphous powder, TG technique was used at a heating rate of 10 °C/min in a nitrogen atmosphere, as shown in Fig. 7. There was a slight weight decrease in the amorphous powder due to the decomposition of impurities adsorbed in the surface. From APTES to PPX-3, the residual weight continued to decline because more organic materials existed outside the powder surface. The values of residual weight for APTES, PPX-1, PPX-2 and PPX-3 at 600 °C were 99.29%, 98.79%, 97.92% and 97.07%, respectively. The inset was the TG curve of PPX film, the initial temperature for weight loss was 410 °C. As the temperature reached 460 °C, which was the annealing temperature of the AMPCs, the remaining weight was still more than 70%. The PPX layers with high thermal stability could perfectly match the requirements of the AMPCs, thus help improve the soft magnetic properties. As the temperature exceeded 600 °C, the TG curve flattened and approached to 0%, PPX has been completely decomposed. The content of PPX layer in PPX-1, PPX-2 and PPX-3 can be estimated from the TG test, and the exact values were 0.50 wt%, 1.37 wt% and 2.22 wt%.

The hysteresis loops of the amorphous powder were presented in Fig. 8. With the increasing thickness of PPX layers, the saturation magnetization (M_s) decreased from 127.9 to 121.5 emu/g since more non-magnetic materials addition. The H_c of these samples was magnified in the inset and was at a similar level, it demonstrated that the ultra-thin

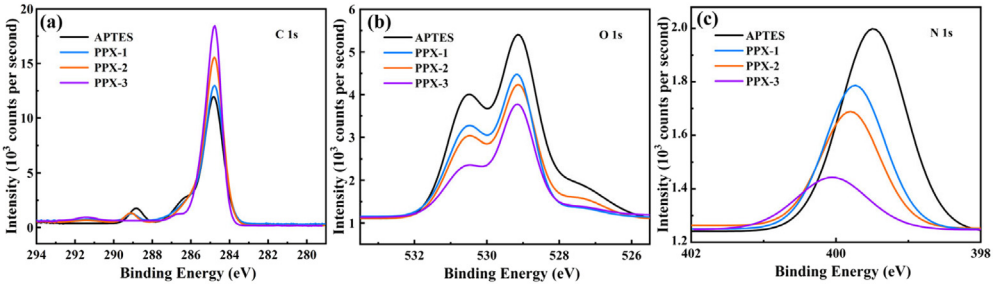

Fig. 5. XPS spectra (a) C 1s, (b) O 1s and (c) N 1s of the powder coated by different layers.

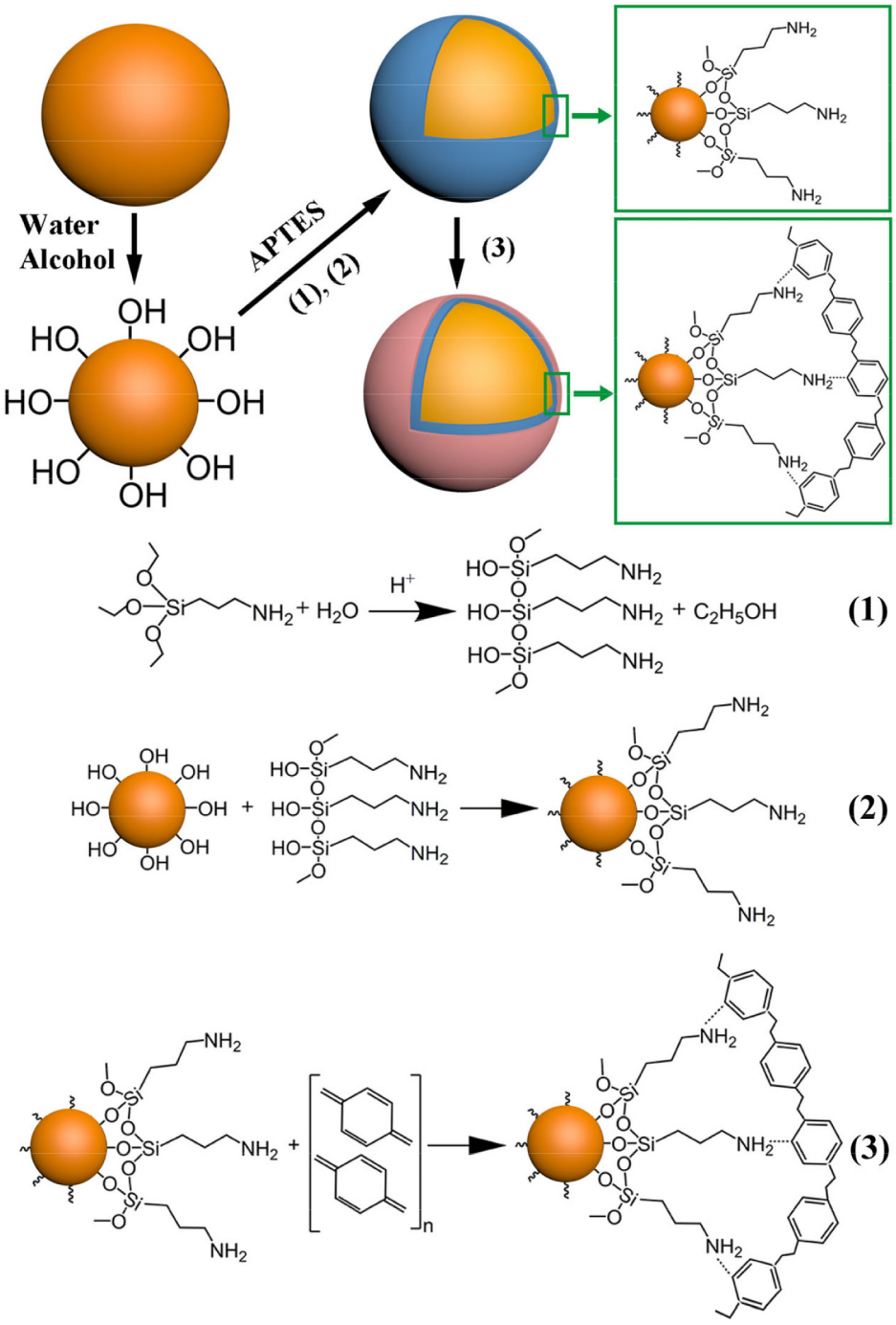

Fig. 6. Schematic drawing and reaction equation of the evolution for coating layer.

PPX coating layer will not deteriorate the H_c. B_s could be calculated by combining M_s and powder's true density ρ as the following equation:

$$B_s = \frac{4\pi\rho M_s}{10^4} \quad (1)$$

For the powder coated by different layers, the true density gradually reduced due to the lower density of PPX layer. The specific values of true density and the calculated B_s of each powder were shown in Table 1.

The thickness of coating layer usually judged by the SEM image of the powder cross-section [32,33], as described before. However, the observed layer thickness is always larger than the actual one. The observed thickness is accurate only when the powder is cut in the middle. In previous researches, several methods have been reported to estimate the layer thickness by considering the core-shell model through M_s, quality, true density and B_s of the powder [22,34]. In the model, the composite powder can be divided into two parts, namely, the core and the shell layer. For a spherical powder with a particle size d (usually refers to the diameter) and layer thickness δ, a following equation is existed to calculate the layer thickness [34,35]:

$$M_{s-comp} = M_{s-core} - \frac{6\delta}{d}(M_{s-core} - M_{s-shell}) \quad (2)$$

where $M_{s\text{-comp}}$ and $M_{s\text{-core}}$ were the saturation magnetization of the amorphous powder before and after coating. $M_{s\text{-shell}}$ was the saturation

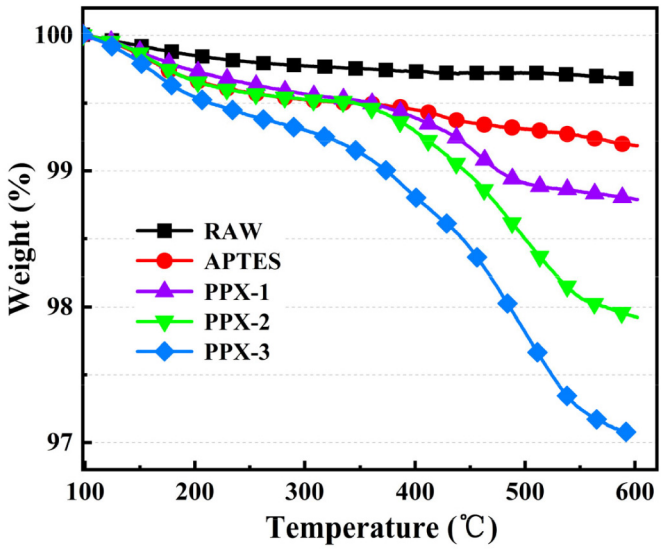

Fig. 7. TG curves of the various amorphous powder, the inset shows the TG curve of PPX layer.

magnetization of coating layer, and for nonmagnetic materials, the $M_{s\text{-shell}}$ could be defined as zero. Therefore, the following equation exists:

$$M_{s-comp} = M_{s-core}\left(1-\frac{6\delta}{d}\right) \tag{3}$$

Considering the values of M_s described before and average particle size ($d = 20.95$ μm) the calculated δ for PPX-1 to PPX-3 were 60, 124 and 178 nm. For thin layer, the value calculated by this formula can be better compounded with the scan results. When the coating layer was thick, the calculated thickness was less than the real value, the reasons can be expressed as follows. This equation originated from the study of size effect on the M_s for nano ferrite particles, it could be well fitted through the studies on the particle size and M_s of ferrite [36–38]. It was more suitable for core-shell structures with a concentrated particle size distribution and a thin shell. For the micron ferromagnetic particles with normal particle size distribution, the calculated value will deviate when the shell is thicker due to the difference in density between the core and shell materials.

The density of particles before and after coating was regarded as approximately equal by Zhang et al. [34]. Considering the quality of the

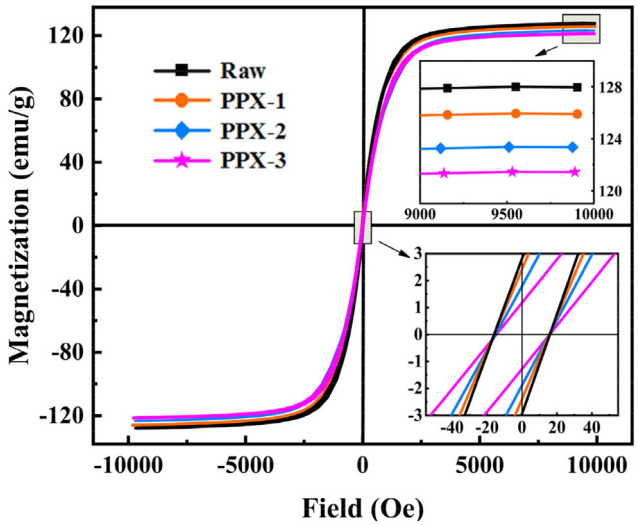

Fig. 8. M-H curves of the amorphous powder and powder coated by different PPX layers.

Table 1
M_s, true density, B_s and calculated layer thickness of different powders.

Sample	M_s (emu/g)	True density (g/cm^3)	B_s (T)	δ calculated through M_s (nm)	δ calculated through density (nm)	δ calculated through B_s (nm)
Raw	128.1	6.87	1.10	–	–	–
PPX-1	125.8	6.69	1.06	60	57	65
PPX-2	122.4	6.47	1.00	125	134	155
PPX-3	121.5	6.23	0.95	180	215	231

magnetic particles before and after coating (marked as m and M), the following equation exists:

$$\frac{M}{\frac{4\pi}{3}(R+\delta)^3} = \frac{m}{\frac{4\pi}{3}R^3} \tag{4}$$

The δ can be calculated as follow:

$$\delta = R\left(\sqrt[3]{\frac{M}{m}}-1\right) \tag{5}$$

However, for magnetic particles composed by organic materials, the true density of particles before and after coating was greatly changed as demonstrated previously. Therefore, this method was suitable for magnetic particles with thin coating layer and little difference in density before and after coating.

Nakahara et al. [22] have reported two effective methods to estimate the thickness of the coating layer. One method is to calculate the coating thickness by using true density of the powder and powder size distribution. The densities of the core and shell could be defined as ρ_{core} and ρ_{shell}, respectively, with the corresponding volumes V_1 and V_2. Then, the density of the composite powder (ρ_{comp}) is given by:

$$\rho_{comp} = \frac{\rho_{core}V_1 + \rho_{shell}V_2}{V_1 + V_2} \tag{6}$$

In general, the radius of a particle was defined as R, then the volume (V_2) of the layer based on the following equation:

$$V_2 = \frac{4\pi}{3}\left[(R+\delta)^3 - R^3\right] \tag{7}$$

Considering Eqs. (6) and (7), the ρ_{comp} could be written as:

$$\rho_{comp} = \frac{\rho_{core}R^3 + \rho_{shell}\left[(R+\delta)^3 - R^3\right]}{(R+\delta)^3} \tag{8}$$

The size distribution is important to take into account, because the same thickness of the coating layer has a greater effect on the density of smaller particles. The particle size distribution of amorphous powder was classified into 25 groups through volume fractions (f_i) and was represented in Supplementary Table 1. The average density considering the size distribution can be written as:

$$\rho_{comp}{}^{-1} = \sum_{i=1}^{25}\frac{f_i V_i}{m_i} = \sum_{i=1}^{25}\frac{f_i}{\rho_i} \tag{9}$$

Combine Eqs. (8) and (9), the equation was as follow:

$$\rho_{comp}{}^{-1} = \sum_{i=1}^{25}\frac{(R_i+\delta)^3 f_i}{R_i^3\cdot\rho_{core} + \left[(R_i+\delta)^3 - R_i^3\right]\rho_{shell}} \tag{10}$$

where R_i was the radius of the original powder and the f_i was the volume fractions of different sizes of powder. The density of PPX film was

1.1 g/cm^3. δ could be calculated by Eq. (10) through MATLAB, the specific values from PPX-1 to PPX-3 were 57, 130, 215 nm, respectively.

B_s of the composite powder also follows the core-shell model, thus, the same principle is applied to estimate the δ and can be expressed as:

$$B_{s-comp}{}^{-1} = \sum_{i=1}^{25} \frac{(R_i+\delta)^3 f_i}{R_i^3 \cdot B_{s-core} + \left[(R_i+\delta)^3 - R_i^3\right] B_{s-shell}} \quad (11)$$

where $B_{s\text{-comp}}$ and $B_{s\text{-core}}$ were the magnetic flux densities of the amorphous powder before and after coating, $B_{s\text{-shell}}$ was the magnetic flux density of the coating layer. For nonmagnetic materials, $B_{s\text{-shell}}$ could be defined as zero. Hence, the calculated δ were 65, 155, 231 nm, respectively. All of the above data can be found in Table 1. The results calculated by density and B_s were closed to those observed in SEM images. Therefore, both of these methods can be well used to judge the thickness of coating layers.

3.3. Soft magnetic properties of the AMPCs

Analysis of the dependence of green density on pressure was presented in Fig. 9(a). The trend of the results illustrated that the green density increased with the increasing pressure. Compared with epoxy resin coating samples, the AMPCs coated by PPX showed higher green density under any pressure. It mainly attributed to the low dynamic friction coefficient of PPX layers [39], which helped to reduce the friction between the powder [20]. However, the large pressure of 2000 MPa caused slight damage to the forming mold. Therefore, the pressure used in subsequent work was 1800 MPa. The relationship between green density, true density and PPX thickness was illustrated in Fig. 9 (b). With increasing the PPX thickness, the true density of the AMPCs decreased. It is because the density of PPX is much smaller than amorphous powder. However, higher PPX thickness gave greater green density as well as lower porosity of the AMPCs thanked to the stronger bonding between the powder. As shown in Fig. 9(c), the ultra-thin PPX-1 layer lead to weak adhesion between powders, thus, it was difficult for the powder to be consolidated into magnetic core. Even if the AMPCs were successfully prepared, cracks were presented inside the magnetic core, leading to a decrease in green density. When PPX layer was thicker, the powder core with larger green density became smooth and crack-free. The high green density meant that the volume fraction of the non-magnetic phase including pores in the powder core was reduced, which was conductive to improve permeability and the whole B_s of AMPCs, resulting in superior soft magnetic properties.

The effective permeability (μ_e) of the AMPCs coated by PPX layers of different thickness was shown in Fig. 10(a). Every sample showed a stable μ_e until 5 MHz, followed by a slight increase and a rapid decline due to ferromagnetic resonance [7]. With the increase thickness of PPX layer, μ_e first increased due to higher green density of the core, then fell because more non-magnetic materials existed. However, the change in μ_e was not obvious, and the specific values of μ_e and green density can be found in Table 2.

In recent years, an increasing number of magnetic devices are required to operate under DC-bias conditions [2]. Therefore, the permeability retention capacity is also an important indicator to measure the performance of the AMPCs under the large bias current. The percent of permeability (%μ) as functions of the DC magnetizing field was shown in Fig. 10(b). For every sample, there was a sustained decrease in μ_e with increasing applied field due to the core saturation, and this trend was non-linear. In a toroidal powder core structure, the internal magnetic path length is shorter than the external one, so the internal magnetic resistance is smaller, resulting in magnetic flux density on the inner magnetic path of the toroidal core becomes higher than that on the outer magnetic path. Therefore, the magnetic flux easily flows into the inner side of the toroidal core and magnetic saturation is generated from the inner magnetic path. Thus, the μ_e value changed non-linearly depending on the instantaneous applied field value [40].

With increasing the thickness of PPX layer, the %μ reduced first and then increased, the values were 52.7%, 50.5% and 54.3% respectively, and PPX-3 exhibited the best DC bias performance. A significant negative association was observed between %μ and μ_e, the results were shown in the inset of Fig. 10(b). The DC bias performance of soft magnetic materials mainly affected by the following aspects. First, a high $\Delta B_{s\text{-}r}$ ($\Delta B_{s\text{-}r} = B_s - B_r$, B_r was remnant magnetization) was required

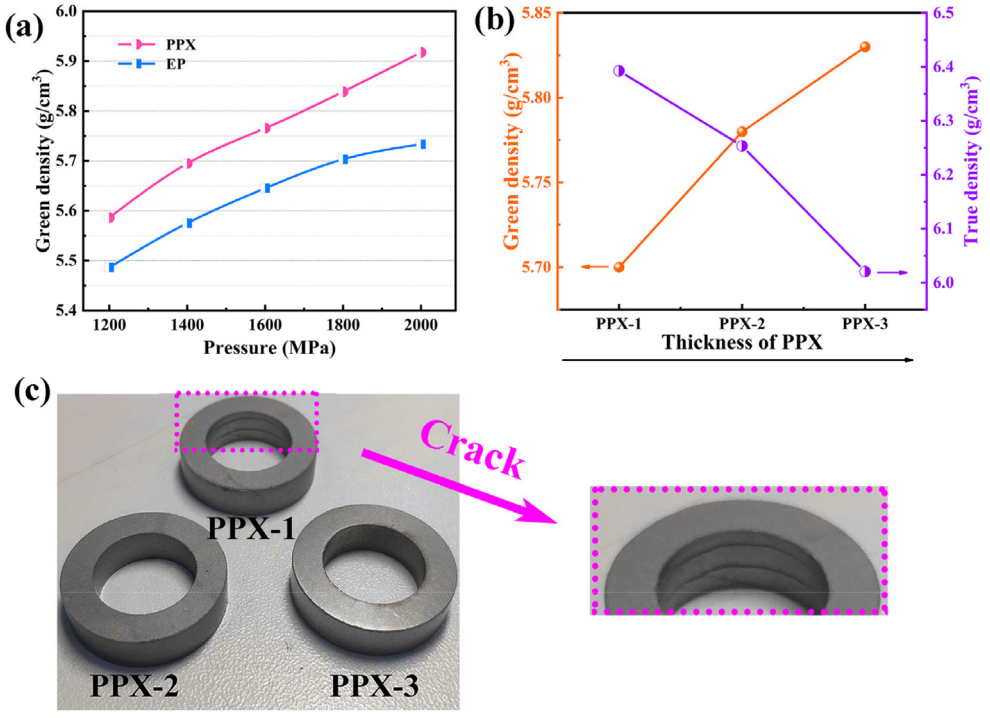

Fig. 9. Green density of the AMPCs coated by (a) PPX and EP in various pressure, (b) green density and true density of AMPCs coated by different thickness of PPX, (c) surface morphology of the AMPCs.

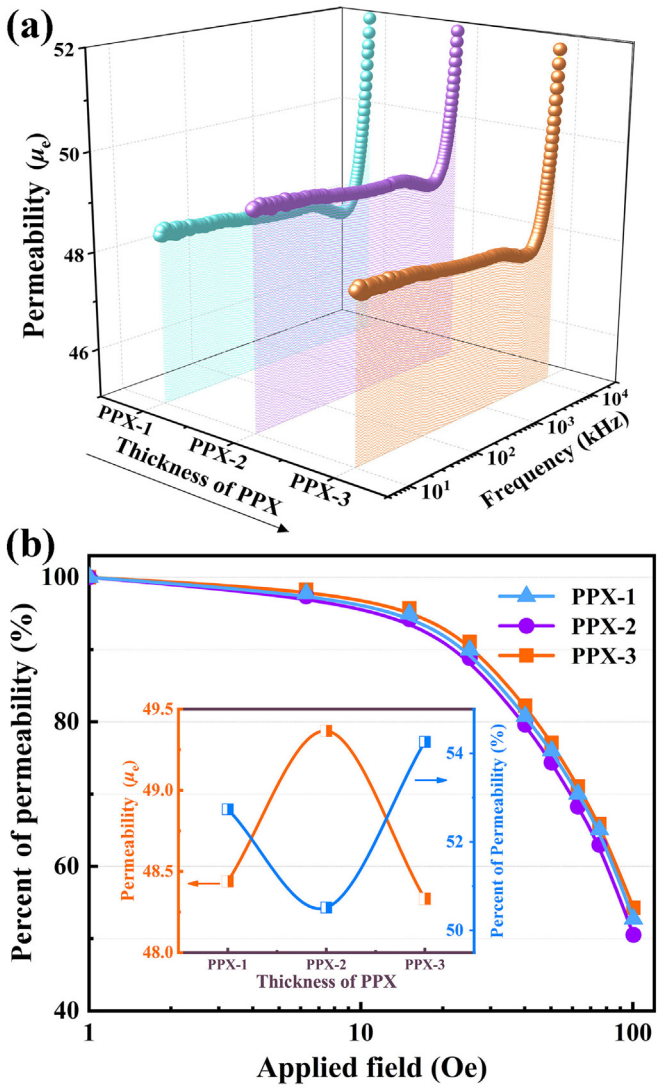

Fig. 10. (a) Effective permeability and (b) DC bias performance of the AMPCs coated by different PPX layers.

because the powder core could be saturated under a large bias field [41]. For soft magnetic materials, the small B_r was usually negligible, hence B_s was particularly important. B_s was proportional to the green density of the AMPCs and M_s of the powder after coating. A thicker coating layer helped to get a higher green density of AMPCs, which was beneficial to obtain a high B_s. However, thicker coating layer also meant more non-magnetic materials were existed, which would weaken the M_s. B_s values of the PPX-1, PPX-2 and PPX-3 were 0.90, 0.87 and 0.89 T, respectively, and was shown in Table 2. The low B_s was one of the reasons that the PPX-2 showed the poor DC bias performance. Second, increasing μ_e reduces the DC bias performance because the magnetic materials saturate at low current. The high μ_e was another reason that the %μ value of PPX-2 was lowest. Furthermore, the structure of the insulating layer between the powder also affected the DC bias characteristics. PPX-1 and PPX-3 showed similar μ_e and B_s, however, the thick and dense PPX-3 layer was beneficial to reduce the effective magnetic field applied on the amorphous powder and enhanced the DC bias performance [30].

Table 2
Green density and soft magnetic properties of the AMPCs coated by PPX, EP and SR.

Sample	Green density (g/cm^3)	B_s (T)	μ_e (100 kHz)	P_{cv} (0.1 T/100 kHz) (mW/cm^3)	DC bias % (100 Oe)
PPX-1	5.70	0.90	48	865	52.7
PPX-2	5.78	0.87	49	795	50.5
PPX-3	5.83	0.89	48	770	54.3
EP (W-6C)	5.72	0.83	54	875	43.9
SR (JM 10)	5.64	0.82	37	1295	63.2
SR (REN 60)	5.34	0.77	36	1360	58.7

One of the key magnetic characteristics of the AMPCs is P_{cv}, the induction and frequency dependence on P_{cv} of the samples were shown in Fig. 11(a). For PPX-1 to PPX-3, P_{cv} gradually reduced under any of the test conditions. Fig. 11(b) showed P_{cv} at the induction of 0.1 T, low P_{cv} of 770 and 1930 mW/cm^3 were obtained for the PPX-3 at 100 and 250 kHz, respectively. In order to find out how P_{cv} reduced, P_h and P_e after loss separation were presented in Fig. 11(c) and (d). Three samples exhibited similar P_h, with PPX-1 being slightly lower. For P_e, a significant decrease occurred with the increasing thickness of PPX layer. It could be considered that the reduction of P_{cv} mainly attributed to the contribution of the P_e.

P_{cv} is usually divided into three parts, including P_h, P_e and P_{ex}, and is generally expressed by the following equation [42].

$$P_{cv} = P_h + P_e + P_{ex} \tag{12}$$

where P_{ex} represents excess losses, is a combination of relaxation and resonant losses of the core which caused mainly by domain wall branching and bowing. Only at very low induction levels or at high frequency levels (near resonance frequency), the value of P_{ex} will become considerable [43]. Therefore, P_{ex} is usually ignored within the usual application frequency range of the AMPCs. P_h dominates in the low frequency range and originates from the rotation of the magnetic domain during magnetization. The value of P_h is proportional to the area of the DC hysteresis loop and can be expressed as the empirical equation:

$$P_h = K_h B_m^{\alpha} f \tag{13}$$

where K_h is the hysteresis coefficient, B_m is the maximum induction, f is the frequency and α is the simulation coefficient. K_h and α closely depend on the H_c of the materials. H_c could be reduced by decreasing impurities in magnetic material, providing a stress relieving heat treatment procedure after the compaction and using smooth and thin insulation coating layers [4]. The amorphous alloy with low H_c is beneficial to reduce the P_h of the AMPCs, as well as the thin and uniform PPX layers. Therefore, the AMPCs with ultra-thin PPX-1 layers exhibited relatively low P_h. P_e dominates at higher frequency range and is proportional to the square of f, is usually consisting of inter-powder eddy current losses (P_{inter}) and intra-powder eddy current losses (P_{intra}), and can be expressed as [43]:

$$P_e = P_{inter} + P_{intra} = \left(\frac{h^2}{\beta\rho_{AMPCs}} + \frac{d}{20\rho_{powder}}\right)\pi^2 {B_m}^2 f^2 \tag{14}$$

where h is the thickness of the samples, d is the powder diameter, β is the geometrical coefficient, ρ_{AMPCs} and ρ_{powder} are the resistivity of the AMPCs and raw amorphous powder. The amorphous powder we used with high resistivity and small powder size, was beneficial to obtain the AMPCs with low P_{intra}. The dense PPX layer without pinhole was totally completely wrapped around the powder, which effectively isolated eddy current paths between the powder. Further increasing the PPX thickness, the ρ_{AMPCs} increased and reduced the P_{inter}, resulting in a reduction in P_{cv}.

The soft magnetic properties of the AMPCs coated by PPX and other commercial high temperature resin were presented in Table 2. Compared with PPX layer, the green density of the AMPCs coated by EP and SR was relatively low. The AMPCs coated by EP showed higher μ_e and P_{cv} due to the poor thermal stability of EP. In addition, this sample exhibited the worst DC bias performance. The AMPCs coated by two types of SR showed very low green density due to the poor adhesive property of SR, it further resulted in the

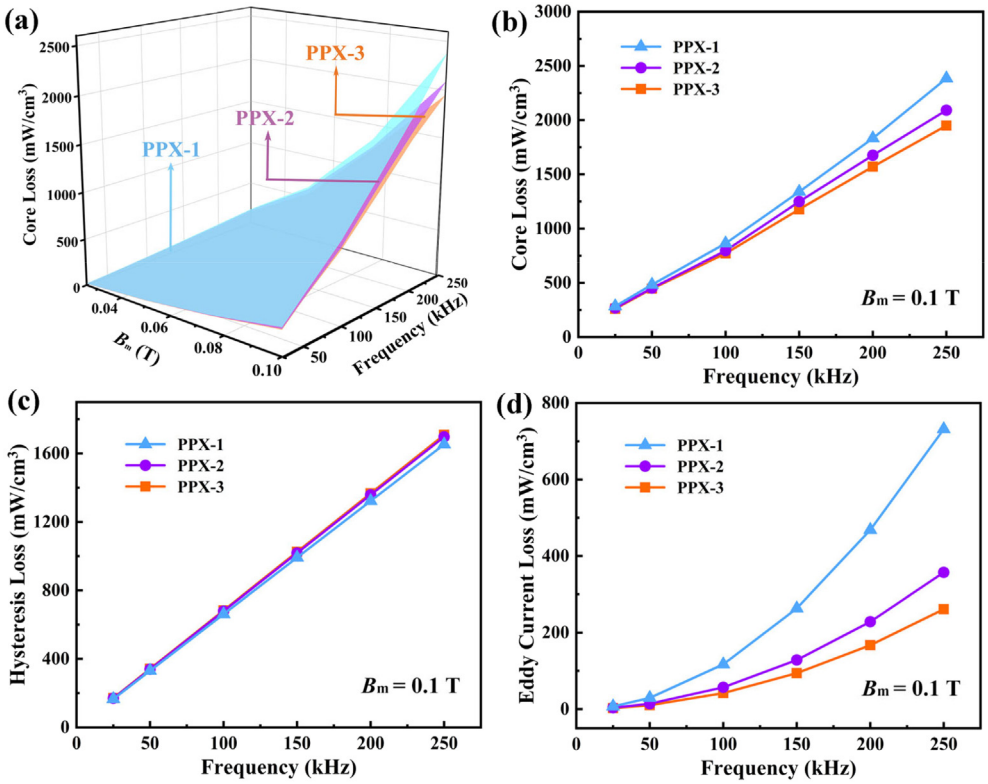

Fig. 11. (a) Core loss of the AMPCs coated by different PPX layers. (b) Core loss, (c) hysteresis loss and (d) eddy current loss of the AMPCs for $B_m = 0.1$ T.

low μ_e and high P_{cv}. In this work, suitable thickness and lubricating PPX-3 coating layer provided excellent soft magnetic properties for the AMPCs with enhanced density, B_s, DC bias performance and lower P_{cv}.

Table 3 summarized the soft magnetic properties of the AMPCs and typical SMCs reported previously. Among them, the Fe and FeSi SMCs show large energy consumption. The FeSiAl SMCs exhibit relatively low P_{cv} but the DC bias performance is undesirable. The FeNiMo SMCs show high μ_e and low P_{cv} but the price is rather unfriendly. Similarly, there are few studies for FeNi SMCs in recent years. The AMPCs with affordable price, low P_{cv} and high B_s, is one of the key development directions of soft magnetic materials in the future. Compared with Tables 2 and 3, the FeSiBPNbCr@SR AMPCs show the high P_{cv}, even higher than FeSi SMCs. The P_{cv} of FeSiBPNbCr@EP AMPCs is similar with FeSiB AMPCs, but the permeability of the former is three times that of the latter. The FeSiBPNbCr@PPX AMPCs fabricated in this work with excellent comprehensive magnetic properties, was a potential candidate for medium and high frequency electric-magnetic devices.

4. Conclusions

In this work, dense, uniform and pinhole-free PPX with high thermal stability and high lubricity has been designed as coating layer for FeSiBPNbCr AMPCs. Three ultra-thin PPX layers have been successfully designed and deposited by CVD. The addition of APTES was conductive to enhance the binding force through the intermolecular interactions between amino and benzene ring, and thus enhance the binding force between PPX layer and amorphous powder. The estimated thickness of the coating layer is more accurate by considering particle size distribution, true density and B_s of the amorphous powder. The average thickness of PPX-1, PPX-2 and PPX-3 was 65, 140 and 240 nm, respectively. The PPX-3 layer provided excellent comprehensive soft magnetic properties for the AMPCs, i.e. stable effective permeability until 5 MHz ($\mu_e = 48$), low total core loss ($P_{cv\ (0.05\ T/100\ kHz)} = 220$ mW/cm^3, $P_{cv\ (0.1\ T/100\ kHz)} = 770$ mW/cm^3) and enhanced DC bias performance ($\mu_{\%\ (100\ Oe)} = 54.3\%$). Compared to commonly used epoxy resins, PPX layer had higher thermal stability and lower dynamic friction coefficient, resulting in higher resistivity and green density of the AMPCs,

Table 3
Comparison of soft magnetic properties of the various SMCs.

Sample		μ_e	P_{cv} (mW/cm^3)		DC bias % (100 Oe)	Ref.
			0.05 T/100 kHz	0.1 T/100 kHz		
Amorphous and nanocrystalline	PPX-3 (This work)	48	220	770	54.3	–
	FeSiBPNbCr@Al_2O_3/EP	52	–	692	46	[21]
	FeSiB@Phenol	19	–	900	–	[11]
	FeSiB+FeNi@SR	31	350	900	–	[44]
	FeSiBPCu@SR	45	–	960		[45]
	FeSiBNbCu@Oxide	40	–	1020	55	[46]
Crystalline	Fe@SiO_2/SR	108	1220	–	–	[47]
	FeSi@Ferrite	110		1190	35	[48]
	FeSiAl@SR	91	178	–	36	[49]
	FeSiCr@Ferrite	50	604	–	–	[33]
	FeNiMo@Chromate	160	–	780		[50]

thus reduced the P_{cv} (12% lower) and enhanced B_s (8.5% enhanced), as well as DC bias performance (24% enhanced).

Supplementary data to this article can be found online at https://doi.org/10.1016/j.matdes.2020.108650.

CRediT authorship contribution statement

Yiqun Zhang: Conceptualization, Formal analysis, Writing - original draft, Writing - review & editing. **Yaqiang Dong:** Conceptualization, Formal analysis, Writing - original draft, Writing - review & editing. **Bang Zhou:** Writing - original draft, Writing - review & editing. **Qiang Chi:** Investigation, Writing - original draft, Writing - review & editing. **Liang Chang:** Investigation, Writing - original draft, Writing - review & editing. **Mengji Gong:** Writing - review & editing, Formal analysis, Writing - original draft. **Jianjun Huang:** Writing - review & editing, Formal analysis, Writing - original draft. **Yan Pan:** Writing - review & editing, Formal analysis, Writing - original draft. **Aina He:** Writing - review & editing, Formal analysis, Writing - original draft. **Jiawei Li:** Writing - review & editing, Formal analysis, Writing - original draft. **Xinmin Wang:** Writing - review & editing, Formal analysis, Writing - original draft.

Declaration of competing interest

The authors declared that they have no conflicts of interest to this work. We declare that we do not have any commercial or associative interest that represents a conflict of interest in connection with the work submitted.

Acknowledgments

This work was supported by the National Key Research and Development Program of China [Grant No. 2016YFB0300500], Ningbo Major Special Projects of the Plan “Science and Technology Innovation 2025” [Grant No. 2018B10062], the Science and Technology Service Network Plan [Grant No. KFJ-STS-SCYD-220], and the National Natural Science Foundation of China [Grant No. 51601205].

References

[1] J.M. Silveyra, E. Ferrara, D.L. Huber, T.C. Monson, Soft magnetic materials for a sustainable and electrified world, Science 362 (2018).
[2] G. Ma, L. Cheng, L.C. Lu, F.Y. Yang, X. Chen, C.Z. Zhu, Effects of DC bias on magnetic performance of high grades grain-oriented silicon steels, J. Magn. Magn. Mater. 426 (2017) 575–579.
[3] C.X. Ouyang, S.M. Xiao, J.H. Zhu, W. Shi, Microwave sintering versus conventional sintering of NiCuZn ferrites. Part II: microstructure and DC-bias superposition characteristics, J. Magn. Magn. Mater. 407 (2016) 182–187.
[4] H. Shokrollahi, K. Janghorban, Soft magnetic composite materials (SMCs), J. Mater. Process. Technol. 189 (2007) 1–12.
[5] P.B. Chen, T. Liu, F.Y. Kong, A.D. Wang, C.Y. Yu, G. Wang, C.T. Chang, X.M. Wang, Ferromagnetic element microalloying and clustering effects in high Bs Fe-based amorphous alloys, J. Mater. Sci. Technol. 34 (2018) 793–798.
[6] G. Herzer, Modern soft magnets: amorphous and nanocrystalline materials, Acta Mater. 61 (2013) 718–734.
[7] E.A. Périgo, B. Weidenfeller, P. Kollár, J. Füzer, Past, present, and future of soft magnetic composites, Appl. Phys. Rev. 5 (2018).
[8] H.X. Li, Z.C. Lu, S.L. Wang, Y. Wu, Z.P. Lu, Fe-based bulk metallic glasses: glass formation, fabrication, properties and applications, Prog. Mater. Sci. 103 (2019) 235–318.
[9] A. Inoue, F.L. Kong, Y. Han, S.L. Zhu, A. Churyumov, E. Shalaan, F. Al-Marzouki, Development and application of Fe-based soft magnetic bulk metallic glassy inductors, J. Alloys Compd. 731 (2018) 1303–1309.
[10] Y.Y. Zheng, Y.G. Wang, Magnetic properties of structure ordered cores composited with $Fe_{78}Si_9B_{13}$ amorphous and pure iron powders, J. Mater. Sci. Mater. Electron. 27 (2015) 2830–2835.
[11] Y.B. Kim, D.H. Jang, H.K. Seok, K.Y. Kim, Fabrication of Fe-Si-B based amorphous powder cores by cold pressing and their magnetic properties, Mater. Sci. Eng. A 449–451 (2007) 389–393.
[12] E.K. Cho, H.T. Kwon, E.M. Cho, Y.S. Song, K.Y. Sohn, W.W. Park, The control of nanograin size and magnetic properties of $Fe_{73}Si_{16}B_7Nb_3Cu_1$ soft magnetic powder cores, Mater. Sci. Eng. A 449–451 (2007) 368–370.
[13] H.B. Sun, C. Wang, W.H. Chen, J.X. Lin, Strategy to enhance magnetic properties of $Fe_{78}Si_9B_{13}$ amorphous powder cores in the industrial condition, Metals 9 (2019) 381.
[14] X.A. Fan, Z.Y. Wu, G.Q. Li, J. Wang, Z.D. Xiang, Z.H. Gan, High resistivity and low core loss of intergranular insulated Fe-6.5wt.%Si/SiO_2 composite compacts, Mater. Des. 89 (2016) 1251–1258.
[15] J.X. Li, J. Yu, W.C. Li, S.L. Che, J.W. Zheng, L. Qiao, Y. Ying, The preparation and magnetic performance of the iron-based soft magnetic composites with the Fe@Fe_3O_4 powder of in situ surface oxidation, J. Magn. Magn. Mater. 454 (2018) 103–109.
[16] H.Y. Chen, J. Lahann, Designable biointerfaces using vapor-based reactive polymers, Langmuir 27 (2011) 34–48.
[17] Z. Hassan, E. Spuling, D.M. Knoll, J. Lahann, S. Brase, Planar chiral [2.2] paracyclophanes: from synthetic curiosity to applications in asymmetric synthesis and materials, Chem. Soc. Rev. 47 (2018) 6947–6963.
[18] H. Hopf, [2.2]Paracyclophanes in polymer chemistry and materials science, Angew. Chem. Int. Ed. 47 (2008) 9808–9812.
[19] H.T. Pu, F.J. Jiang, Y.X. Wang, B. Yan, Soft magnetic composite powders of reduced iron coated with poly(p-xylylene) via chemical vapor deposition polymerization, Colloids Surf. A Physicochem. Eng. Asp. 361 (2010) 62–65.
[20] S. Wu, A.Z. Sun, Z.W. Lu, C. Cheng, Fabrication and properties of iron-based soft magnetic composites coated with parylene via chemical vapor deposition polymerization, Mater. Chem. Phys. 153 (2015) 359–364.
[21] Y.Q. Zhang, Y.Q. Dong, L. Liu, L. Chang, B. Zhou, Q. Chi, X.M. Wang, High filling alumina/epoxy nanocomposite as coating layer for Fe-based amorphous powder cores with enhanced magnetic performance, J. Mater. Sci. Mater. Electron. 30 (2019) 14869–14877.
[22] S. Nakahara, E.A. Périgo, Y. Pittini-Yamada, Y. de Hazan, T. Graule, Electric insulation of a FeSiBC soft magnetic amorphous powder by a wet chemical method: identification of the oxide layer and its thickness control, Acta Mater. 58 (2010) 5695–5703.
[23] Y. Pittini-Yamada, E.A. Périgo, Y. de Hazan, S. Nakahara, Permeability of hybrid soft magnetic composites, Acta Mater. 59 (2011) 4291–4302.
[24] Y.D. Peng, T. Yi, L.Y. Li, J.H. Yi, J.W. Nie, C.X. Bao, Iron-based soft magnetic composites with Al_2O_3 insulation coating produced using sol-gel method, Mater. Des. 109 (2016) 390–395.
[25] H.T. Pu, Y.X. Wang, Z.L. Yang, Chemical vapor deposition copolymerization of 4-carboxyl-[2,2] paracyclophane and 4-amino-[2,2] paracyclophane, Mater. Lett. 61 (2007) 2718–2722.
[26] H. Torii, M. Tasumi, Intermolecular hydrogen bonding and low-wave-number vibrational spectra of formamide, N-methylformamide, and N-methylacetamide in the liquid state, Int. J. Quantum Chem. 70 (1998) 241–252.
[27] J.M. Hill, D.G. Royce, C.S. Fadley, L.F. Wagner, F.J. Grunthaner, Properties of oxidized silicon as determined by angular-dependent X-ray photoelectron spectroscopy, Chem. Phys. Lett. 44 (1976) 225–231.
[28] S.F. Lomayeva, A.V. Syugaev, A.N. Maratkanova, A.A. Shakov, K.N. Rozanov, D.A. Petrov, C.A. Stergiou, Structure and microwave properties of Fe powders prepared by surfactant-assisted ball milling in organic media, J. Alloys Compd. 721 (2017) 18–27.
[29] D.W. Zeng, K.C. Yung, C.S. Xie, XPS investigation of the chemical characteristics of Kapton films ablated by a pulsed TEA CO_2 laser, Surf. Coat. Technol. 153 (2002) 210–216.
[30] F. Luo, X.A. Fan, Z.G. Luo, W.T. Hu, J. Wang, Z.Y. Wu, G.Q. Li, Y.W. Li, X. Liu, Microstructure, formation mechanism and magnetic properties of $Fe_{1.82}Si_{0.18}$@Al_2O_3 soft magnetic composites, J. Magn. Magn. Mater. 493 (2020) 165744.
[31] N. Solcà, O. Dopfer, IR spectrum of the benzene-water cation: direct evidence for a hydrogen-bonded charge-dipole complex, Chem. Phys. Lett. 347 (2001) 59–64.
[32] B. Zhou, Y.Q. Dong, L. Liu, Q. Chi, Y.Q. Zhang, L. Chang, F.Q. Bi, X.M. Wang, The core-shell structured Fe-based amorphous magnetic powder cores with excellent magnetic properties, Adv. Powder Technol. 30 (2019) 1504–1512.
[33] S. Mori, T. Mitsuoka, K. Sugimura, R. Hirayama, M. Sonehara, T. Sato, N. Matsushita, Core-shell structured Mn-Zn-Fe ferrite/Fe-Si-Cr powders for magnetic composite cores with low loss, Adv. Powder Technol. 29 (2018) 1481–1486.
[34] Q. Zhang, W. Zhang, K. Peng, In-situ synthesis and magnetic properties of core-shell structured Fe/Fe_3O_4 composites, J. Magn. Magn. Mater. 484 (2019) 418–423.
[35] J. Li, X. Wang, X. Xu, R. Gong, Z. Feng, Y. Chen, V.G. Harris, Low power loss and field-insensitive permeability of Fe-6.5%Si powder cores with manganese oxide-coated particles, J. Appl. Phys. 117 (2015) 17D518.
[36] A.E. Berkowitz, W.J. Schuele, P.J. Flanders, Influence of crystallite size on the magnetic properties of acicular γ-Fe_2O_3 particles, J. Appl. Phys. 39 (1968) 1261–1263.
[37] J.P. Chen, C.M. Sorensen, K.J. Klabunde, G.C. Hadjipanayis, E. Devlin, A. Kostikas, Size-dependent magnetic properties of $MnFe_2O_4$ fine particles synthesized by coprecipitation, Phys. Rev. B 54 (1996) 9288–9296.
[38] Z.W. Li, L. Chen, C.K. Ong, Z. Yang, Static and dynamic magnetic properties of Co_2Z barium ferrite nanoparticle composites, J. Mater. Sci. 40 (2005) 719–723.
[39] T. Goda, T. Konno, M. Takai, K. Ishihara, Photoinduced phospholipid polymer grafting on Parylene layer: advanced lubrication and antibiofouling properties, Colloids Surf. B Biointerfaces 54 (2007) 67–73.
[40] J. Imaoka, K. Okamoto, M. Shoyama, Y. Ishikura, M. Noah, M. Yamamoto, Modeling, magnetic design, simulation methods, and experimental evaluation of various powder cores used in power converters considering their DC superimposition characteristics, IEEE Trans. Power Electron. 34 (2018) 9033–9051.
[41] K. Sun, G.H. Wu, B. Wang, Q.Y. Zhong, Y. Yang, Z. Yu, C.J. Wu, P.W. Wei, X.N. Jiang, Z.W. Lan, Cation distribution and magnetic property of Ti/Sn-substituted manganese-zinc ferrites, J. Alloys Compd. 650 (2015) 363–369.
[42] B. Yang, X.P. Li, R.Y. Guo, R.H. Yu, Oxidation fabrication and enhanced soft magnetic properties for core-shell FeCo/$CoFe_2O_4$ micron-nano composites, Mater. Des. 121 (2017) 272–279.
[43] P. Kollár, Z. Birčáková, J. Füzer, R. Bureš, M. Fáberová, Power loss separation in Fe-based composite materials, J. Magn. Magn. Mater. 327 (2013) 146–150.

[44] B. Li, Z.G. Zheng, H.Y. Yu, D.C. Zeng, Improved permeability of Fe based amorphous magnetic powder cores by adding Permalloy, J. Magn. Magn. Mater. 438 (2017) 138–143.
[45] J. Luan, P. Sharma, N. Yodoshi, Y. Zhang, A. Makino, Mechanically strong nanocrystalline Fe-Si-B-P-Cu soft magnetic powder cores utilizing magnetic metallic glass as a binder, AIP Adv. 6 (2016), 055934.
[46] T.H. Kim, K.K. Jee, Y.B. Kim, D.J. Byun, J.H. Han, High-frequency magnetic properties of soft magnetic cores based on nanocrystalline alloy powder prepared by thermal oxidation, J. Magn. Magn. Mater. 322 (2010) 2423–2427.
[47] C. Wu, M.Q. Huang, D.H. Luo, Y.Z. Jiang, M. Yan, SiO_2 nanopowders enhanced silicone resin as the matrix for Fe soft magnetic composites with improved magnetic, mechanical and thermal properties, J. Alloys Compd. 741 (2018) 35–43.
[48] M.M. Zhou, Y. Han, W.W. Guan, S.J. Han, Q.S. Meng, T.T. Xu, H.L. Su, X. Guo, Z.Q. Zou, F.Y. Yang, Y.W. Du, Magnetic properties and loss mechanism of Fe-6.5wt%Si powder core insulated with magnetic Mn-Zn ferrite nanopowders, J. Magn. Magn. Mater. 482 (2019) 148–154.
[49] R.R. Bai, Z.H. Zhu, H. Zhao, S.H. Mao, Q. Zhong, The percolation effect and optimization of soft magnetic properties of FeSiAl magnetic powder cores, J. Magn. Magn. Mater. 433 (2017) 285–291.
[50] Z.M. Zhang, W. Xu, T. Guo, Y.Z. Jiang, M. Yan, Effect of processing parameters on the magnetic properties and microstructures of molybdenum permalloy compacts made by powder metallurgy, J. Alloys Compd. 594 (2014) 153–157.